

University of Groningen

Reversible oxygen migration and phase transitions in hafnia-based ferroelectric devices

Nukala, Pavan; Ahmadi, Majid; Wei, Yingfen; Graaf, Sytze de; Stylianidis, Evgenios; Chakraborty, Tuhin; Matzen, Sylvia; Zandbergen, Henny W.; Björling, Alexander; Mannix, Dan

Published in:
Science

DOI:
[10.1126/science.abf3789](https://doi.org/10.1126/science.abf3789)

IMPORTANT NOTE: You are advised to consult the publisher's version (publisher's PDF) if you wish to cite from it. Please check the document version below.

Document Version
Publisher's PDF, also known as Version of record

Publication date:
2021

[Link to publication in University of Groningen/UMCG research database](#)

Citation for published version (APA):

Nukala, P., Ahmadi, M., Wei, Y., Graaf, S. D., Stylianidis, E., Chakraborty, T., Matzen, S., Zandbergen, H. W., Björling, A., Mannix, D., Carbone, D., Kooi, B., & Noheda, B. (2021). Reversible oxygen migration and phase transitions in hafnia-based ferroelectric devices. *Science*, 372(6542), 630-635.
<https://doi.org/10.1126/science.abf3789>

Copyright

Other than for strictly personal use, it is not permitted to download or to forward/distribute the text or part of it without the consent of the author(s) and/or copyright holder(s), unless the work is under an open content license (like Creative Commons).

The publication may also be distributed here under the terms of Article 25fa of the Dutch Copyright Act, indicated by the "Taverne" license. More information can be found on the University of Groningen website: <https://www.rug.nl/library/open-access/self-archiving-pure/taverne-amendment>.

Take-down policy

If you believe that this document breaches copyright please contact us providing details, and we will remove access to the work immediately and investigate your claim.

Downloaded from the University of Groningen/UMCG research database (Pure): <http://www.rug.nl/research/portal>. For technical reasons the number of authors shown on this cover page is limited to 10 maximum.

FERROELECTRICS

Reversible oxygen migration and phase transitions in hafnia-based ferroelectric devices

Pavan Nukala^{1,2*}, Majid Ahmadi^{1,3}, Yingfen Wei^{1,3}, Sytze de Graaf¹, Evgenios Stylianidis^{1,4}, Tuhin Chakraborty², Sylvia Matzen⁵, Henny W. Zandbergen⁶, Alexander Björling⁷, Dan Mannix^{8,9,10}, Dina Carbone⁷, Bart Kooi^{1,3}, Beatriz Noheda^{1,3*}

Unconventional ferroelectricity exhibited by hafnia-based thin films—robust at nanoscale sizes—presents tremendous opportunities in nanoelectronics. However, the exact nature of polarization switching remains controversial. We investigated a $\text{La}_{0.67}\text{Sr}_{0.33}\text{MnO}_3/\text{Hf}_{0.5}\text{Zr}_{0.5}\text{O}_2$ capacitor interfaced with various top electrodes while performing in situ electrical biasing using atomic-resolution microscopy with direct oxygen imaging as well as with synchrotron nanobeam diffraction. When the top electrode is oxygen reactive, we observe reversible oxygen vacancy migration with electrodes as the source and sink of oxygen and the dielectric layer acting as a fast conduit at millisecond time scales. With nonreactive top electrodes and at longer time scales (seconds), the dielectric layer also acts as an oxygen source and sink. Our results show that ferroelectricity in hafnia-based thin films is unmistakably intertwined with oxygen voltammetry.

The discovery of silicon-compatible nanoferroelectricity in hafnia-based thin films (1) has triggered a vast amount of fundamental research and has rejuvenated interest in ferroelectric materials in microelectronics, for both low-power, nonvolatile memory and logic devices. This ferroelectricity is robust even at film thicknesses as low as 1 nm (2–4), a situation that was believed to be impossible on the basis of the classical understanding of ferroelectricity. The spontaneous polarization observed in these films is ascribed generally to a metastable polar orthorhombic (o-) phase (*Pca2₁*) (5). A higher-energy rhombohedral (r-) phase (*R3m/R3*) has been reported for epitaxial growth of $\text{Hf}_{0.5}\text{Zr}_{0.5}\text{O}_2$ (HZO) on $\text{La}_{0.67}\text{Sr}_{0.33}\text{MnO}_3$ (LSMO)-buffered perovskite and on trigonal substrates (6). Remnant polarization (P_r) values as high as 35 $\mu\text{C}/\text{cm}^2$ were measured (7) on HZO. The pronounced effects of particle size reduction, surface effects, dopants, oxygen vacancies (\dot{V}_o), epitaxial strain, and residual stresses at the nanoscale have been investigated as possible reasons to stabilize these otherwise metastable phases in thin films (5, 8, 9). On the

other end of the size range, films as thick as 1 μm (10) and bulk samples (11) are ferroelectric, with the stabilization resulting from dopant and defect chemistry (10, 12).

Armed with an understanding of the virgin state polarization, research is being conducted on the mechanism of polarization switching. The dynamics of this process, through the lens of a nucleation-limited switching model and pointing out the negligible role of domain growth (or domain wall motion), have been studied for doped hafnia films grown in the o-phase (13–19). Flat phonon bands and localized dipoles in half unit cells in the o-phase have been postulated as an intrinsic reason for switching without forming domain walls in these systems (20).

Hafnia-based and zirconia-based materials are also an important class of resistive memory devices and oxygen conductors that exhibit memristive hysteresis driven by \dot{V}_o conduction and redox reactions (21, 22). More generally, in devices of thin-film ferroelectric oxides such as tunnel junctions, both \dot{V}_o migration and polarization switching lead to hysteresis (23–28). Understanding whether these effects are synergistic or independent is crucial to achieve device control (29–33). In tunnel junctions of HZO thin films on LSMO-buffered SrTiO_3 (STO), Wei *et al.* (23) observed a divergence of the tunnel electroresistance (TER) from 100% to 10⁶% upon device cycling, which the authors explained as a possible transition from polarization switching to \dot{V}_o migration-assisted switching. This observation suggested that the two mechanisms are independent. Sulzbach *et al.* (24) have also reported a similar divergence in the TER as a function of the applied voltage in HZO layers before breakdown. On the other hand, the electric polarization in hafnia has been theoretically proposed to originate from oxygen vacancies through electro-

strictive effects, which strongly suggests the extrinsic nature of the polarization switching (29). Direct structural observations during polarization switching can potentially resolve these controversies (34).

We report operando atomic-scale electron microscopy investigations of LSMO/HZO/LSMO capacitor stacks grown on conducting (Nb-doped) STO substrate under an electric field (35). LSMO is a standard choice of bottom electrode in complex oxide devices (23–26, 31), so our conclusions are relevant for understanding a wider class of devices. We performed in situ biasing measurements while employing two scanning transmission electron microscopy (STEM) imaging modes—high-angle annular dark field (HAADF)–STEM and integrated differential phase contrast (iDPC)–STEM. With iDPC–STEM, we recently imaged H atoms next to Ti metal atoms (36), demonstrating that this is a robust atomic-resolution imaging technique for simultaneously measuring heavy and light elements. By directly imaging oxygen, we provide evidence of the reversible and hysteretic migration of \dot{V}_o from the bottom to the top electrode through the HZO layer. Associated with such migration, we show that \dot{V}_o induce phase transitions in the LSMO (bottom electrode) and HZO layers. Additionally, through operando x-ray diffraction, ex situ microscopy, and transport measurements on devices with both noble (Au) and oxygen reactive top electrodes (LSMO and TiN), we show that oxygen voltammetry is also found at short time scales (millisecond and less). We believe these observations clearly show that polarization switching and oxygen voltammetry are not independent.

We begin by showing the evolution of the epitaxial LSMO layer (bottom electrode), with the voltage applied to the top electrode and keeping the bottom electrode at 0 V (fig. S1) (22). Our iDPC–STEM image of the virgin state (Fig. 1A and fig. S2A) shows the antiphase octahedral δ tilts present in the LSMO perovskite structure (22). Mn–O–Mn bond angles, as we measured in various regions, are between 165° and 176° (37). Upon increasing the bias to 2 V, a noticeable displacement of Mn columns away from the center of the oxygen octahedra (Fig. 1B) appears throughout the film (barring the first three monolayers at the interface with Nb:STO). These displacements are randomly oriented with a mean value of 18.6 pm and standard deviation of 10.2 pm (fig. S3), which indicates a transformation from an MnO_6 octahedral toward an MnO_5 square pyramidal coordination (35). Thus at 2 V, the LSMO film contains a combination of MnO_5 and MnO_6 polyhedra. Although this structural feature was not previously observed for LSMO, Brownmillerite [(BM), oxygen-deficient perovskite] phases are reported to exhibit MnO_5 square pyramids in the parent

¹Zernike Institute of Advanced Materials, University of Groningen, 9747 AG Groningen, Netherlands. ²Centre for Nano Science and Engineering, Indian Institute of Science, Bengaluru, 560012, India. ³CogniGron (Groningen Cognitive Systems and Materials Center), University of Groningen, 9747 AG Groningen, Netherlands. ⁴Department of Physics and Astronomy, University College London, London WC1E 6BT, UK. ⁵Center for Nanoscience and Nanotechnology, Paris-Saclay University, CNRS, 91120 Palaiseau, France. ⁶Kavli Institute of Nanoscience, Faculty of Applied Sciences, Delft University of Technology, 2628 CJ Delft, Netherlands. ⁷MAX IV Laboratory, Lund University, SE-221 00 Lund, Sweden. ⁸University Grenoble Alpes, CNRS, Institut Néel, 38042 Grenoble, France. ⁹European Spallation Source, SE-221 00 Lund, Sweden. ¹⁰Department of Chemistry, Aarhus University, DK-8000 Aarhus, Denmark.
*Corresponding author. Email: pnukala@iisc.ac.in (P.N.); b.noheda@rug.nl (B.N.)

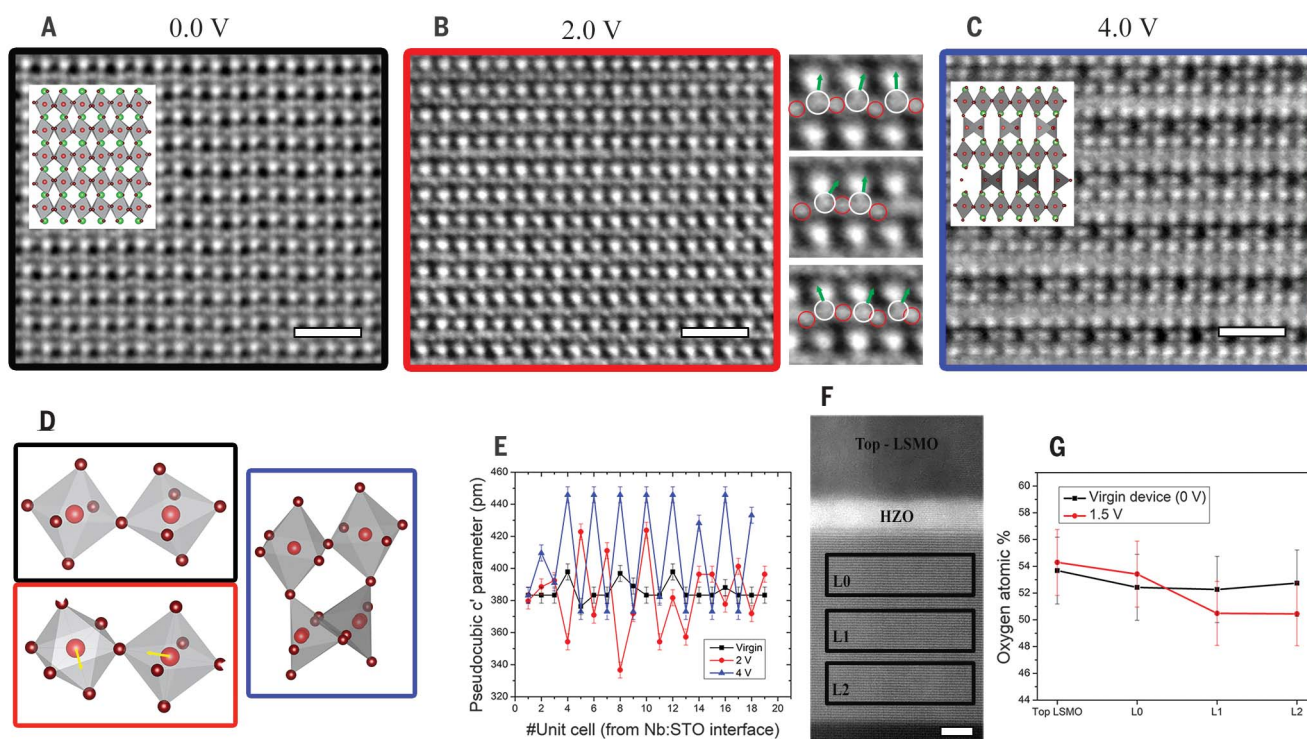


Fig. 1. Deoxygenation of bottom electrode LSMO layer with increasing positive bias. (A) iDPC-STEM image of a representative region of the bottom LSMO layer in the virgin state, viewed along the [110] zone axis, exactly matching the perovskite structure. Schematic in the inset shows MnO₆ octahedra and their antiphase tilts, clearly imaged in (A). In the inset, La/Sr is green, Mn is red, and O is brown. (B) iDPC-STEM image at $V = 2$ V. Panels on the right show various unit cells, illustrating Mn columns (circled in white) and their displacements (marked by green arrows) away from the center of an octahedron. Oxygen columns are marked in red circles. (C) iDPC-STEM at 4 V. BM LSMO (zone axis:

a ; schematic in inset) denoted by alternating MnO₄ tetrahedra and MnO₆ octahedra along c' . (D) Schematic showing the evolution of an MnO₆ octahedra in the virgin state (enclosed in black box), toward MnO₅ square pyramids at 2 V (enclosed in red box), to alternating MnO₄ tetrahedra and MnO₆ octahedra at 4 V (enclosed in blue box). (E) Plot of variation of c' (La-La distance) parameter from the STO interface in perovskite (black), BM-precursor (red), and BM phases (blue). (F and G) Overview image of LSMO/HZO/LSMO capacitor (F) with regions marked where oxygen content was quantified from EDS (G) at 0 V and 1.5 V. Scale bars, 1 nm in (A) to (C) and 5 nm in (F).

compound, SrMnO₃ (38). We refer to this MnO₅-MnO₆ combination as a BM-precursor phase (39). As for the first three monolayers, an important feature is the exaggerated antiphase δ tilts, with Mn-O-Mn bond angles of 143° to 146° that are not typical of perovskite structures (fig. S2, B to D).

Upon increasing the biasing voltage to 4 V, LSMO converts into a well-studied BM phase (40, 41) except for the first few monolayers near the interface with the substrate, which transform to the BM-precursor phase (fig. S4A). Transformation from perovskite to the BM phase occurs through \tilde{V}_0 ordering in every alternate Mn-O plane along the c' -axis (Fig. 1C), transforming the Mn coordination from octahedral or square pyramidal to tetrahedral. Back-to-back MnO₄ tetrahedra in [1-10] alternate with MnO₆ octahedra along c' , indicating the BM phase (Fig. 1C). This transformation is hysteretic and nonvolatile, with LSMO remaining in the BM phase even when the external bias is removed (fig. S4) (35).

The multiple-step transformations (Fig. 1D) from MnO₆ octahedra (virgin state) toward square pyramids plus octahedra (2 V), to alternating octahedra and tetrahedra (4 V) also correlate to the variation of the pseudocubic lattice parameter along the electric-field direction (called c'). We determined the c' values at various bias voltages for the first 20 monolayers in LSMO starting from the Nb:STO interface (Fig. 1E). In the virgin state, we measured c' to be 384 (± 5) pm with \tilde{V}_0 disorder-induced expansion in some planes (35). At 2 V, c' oscillates with values between 335 and 425 pm, without any superstructure. At 4 V, except for the first few monolayers, c' alternates between 375 and 445 pm, doubling the lattice periodicity. Energy-dispersive spectroscopy (EDS) (35) reveals a clear gradient of oxygen concentration in the bottom electrode compared with the virgin state, even at a low bias of 1.5 V, with more \tilde{V}_0 occurring closer to the Nb:STO interface (Fig. 1, F and G).

Notably, the BM phase can be reoxygenated when negative voltages are applied to the top

electrode. We show that this takes place for biases as low as -1 V (fig. S5A). The hysteretic BM phase clearly begins to reoxygenate in iDPC-STEM images of the same field of view at 0 and -1.3 V (Fig. 2, A and B), with the appearance of extra oxygen columns at -1.3 V in the Mn-O planes that were oxygen deficient at 0 V (fig. S5A). Upon ramping the bias to -3 V, the entire layer converts to the BM-precursor phase (Fig. 2C), which is retained also when the bias is removed (Fig. 2D), as we confirmed by the corresponding disorderly c' variation (fig. S5B).

To address the time scales of the processes associated with de- and reoxygenation of LSMO layers, we followed the dynamics through HAADF-STEM image acquisition, after poling at -4 V (transforming LSMO completely back to the starting perovskite phase). Upon increasing the bias to 3 V (Fig. 2E), the initial perovskite phase changes to the BM-precursor phase in 60 s and then to the BM phase within 120 s. These changes are indicated by the variations we observe in the c' parameter. By applying

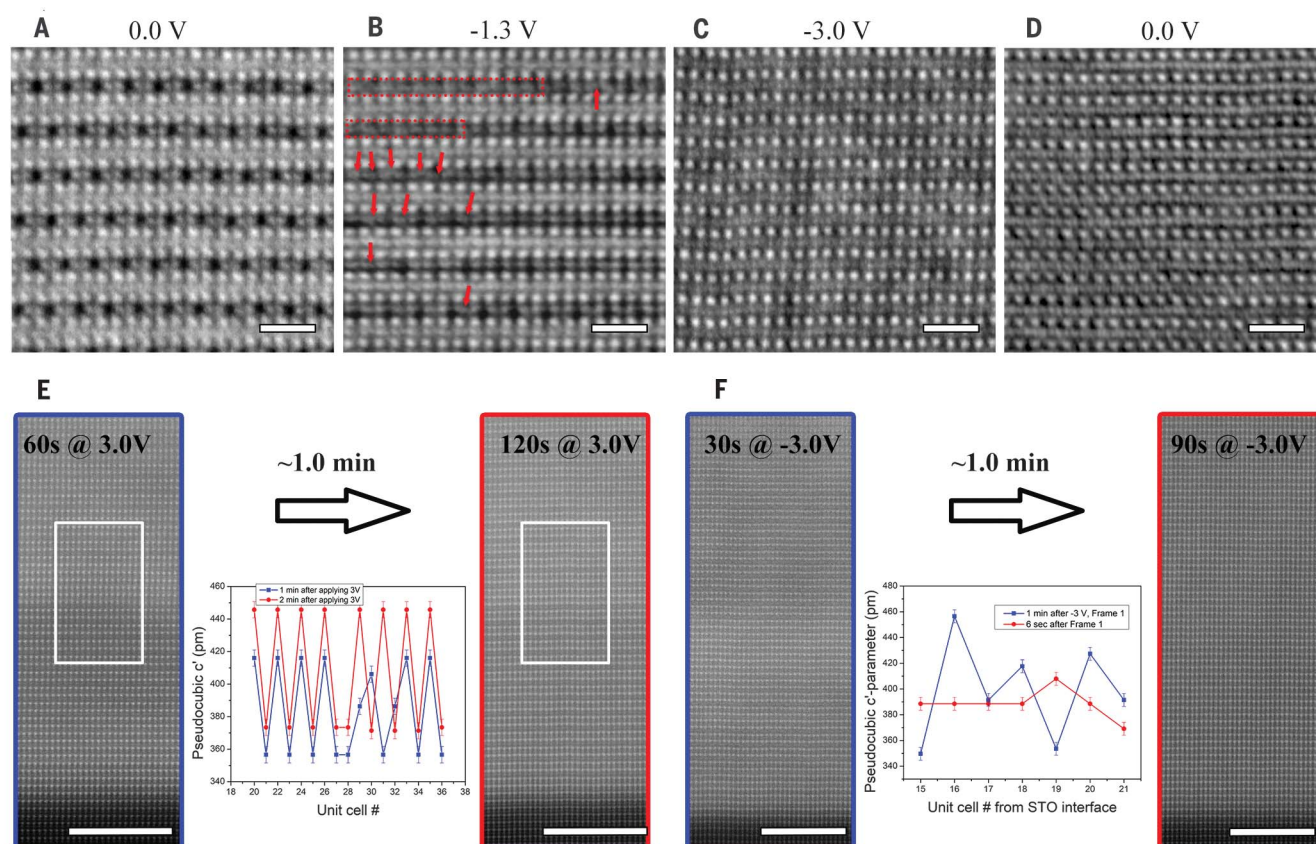


Fig. 2. Oxygenation of bottom electrode LSMO layer with increasing negative bias. (A and B) iDPC-STEM images of a region in the same field of view at 0 (A) and -1.3 V (B). At -1.3 V, oxygen columns start to appear (marked by red arrows) in positions where there were none in the BM phase at 0 V. (C and D) BM phase transforms to BM-precursor phase at -3 V (C) and is retained so at 0 V (D). (E) Dynamics are recorded through HAADF-STEM imaging within 120 s of ramping from 0 to 3 V from a starting perovskite phase. A

BM-precursor phase is imaged at 60 s, and a BM phase is imaged at 120 s. (F) Upon changing the bias to -3 V, a BM phase is recorded at 30 s that changes to a perovskite phase by 90 s (for disappearance of the superstructure spots in FFT, see fig. S4). The intermediate BM-precursor phase recorded at 60 s converts to a perovskite-like phase in ~ 6 s, as can be seen by the variation in the c' parameter, which gives an idea about the time scales of \tilde{V}_o migration. Scale bars, 1 nm in (A) to (D) and 5 nm in (E) and (F).

-3 V, a complete transformation from a BM phase back to perovskite phase occurs within 90 s in the region [Fig. 2F; fast Fourier transform (FFT) in fig. S5C]. We then follow the same region for 10 s using a faster HAADF-STEM image series (1.2 s per frame). From the c' parameter variations, we conclude that the BM-precursor phase transformed to the perovskite phase (Fig. 2F, center panel). Thus, although the complete transformation from perovskite to BM and back takes about a couple of minutes at 3 and -3 V, \tilde{V}_o migration and partial phase-transitions already start occurring in time scales of seconds at these voltages. At 2 V, however, the partial transition to the BM-precursor phase itself takes 3 to 4 hours. The change in kinetics with voltage is consistent with the ultra-nonlinear voltage-time dilemma typically observed in oxide-resistive memories (42). Thus, we expect that at higher voltages these mechanisms will occur at very short time scales.

We also monitored the structural evolution in the HZO (6 nm) layer under the application of bias. From the multislice iDPC-STEM image simulations for HZO [see also (43)] in the r-phase ($R3m$) with [111] out-of-plane (Fig. 3A, inset), we recognize the (001) planes (at $\sim 55^\circ$ with respect to the [111] direction) by cationic (Hf/Zr) columns surrounded by two oxygen columns on either side of them. In the virgin state, our experimental images perfectly match the r-phase simulations. We followed the evolution of a supercell (Fig. 3A) in this grain upon application of bias along the out-of-plane [111] direction. We show the displacement of \tilde{V}_o for this supercell occurs (35) (fig. S6A) with respect to the 0-V configuration in Fig. 3B. While \tilde{V}_o migrate toward the bottom electrode with increasing bias (Fig. 3B), they also gather some in-plane displacement (Fig. 3B, inset).

At 4 V, the same grain transforms into a combination of multiple grains (Fig. 3C). Upon

inspecting various regions in the film, we found that the majority of the grains have changed their structure from r-phase to the more thermodynamically stable o- and monoclinic (m-) phases (Fig. 3D and fig. S6C). The o-phase is commonly observed in ferroelectric HZO layers grown by various methods (5), whereas the r-phase is only observed under specific growth procedures and conditions (6). Our observations on HZO point to the r-phase being stabilized under slightly oxygen-deficient conditions. Replenishment of oxygen in the HZO layer under bias (originating from the bottom LSMO layer) transforms it into more stoichiometric m- or o-phases. The \tilde{V}_o in the HZO layer, and thus the r-phase, is restored (by reverse migration) upon applying a bias of -3 V, as can be seen from the perfect match of the experimental iDPC-STEM of two representative domains (180° rotated from each other) (Fig. 3E) with the multislice image simulations (Fig. 3A, inset).

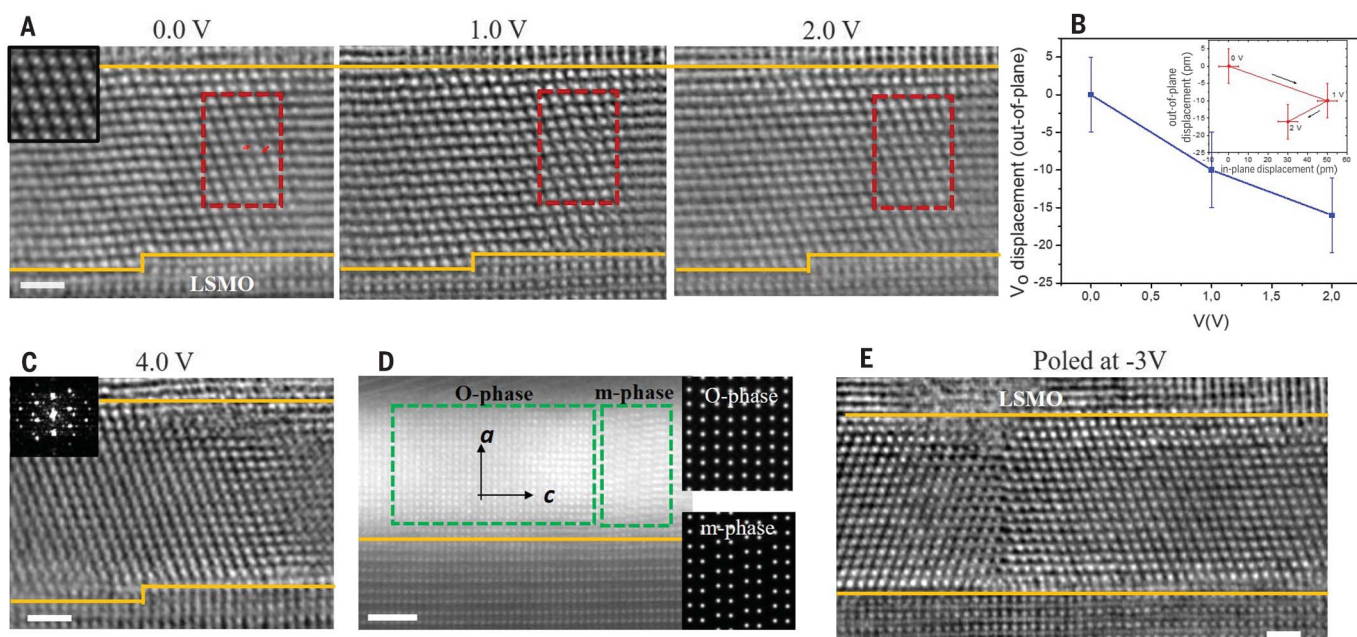


Fig. 3. Oxygenation and deoxygenation of HZO and associated phase transitions. (A) Evolution of an r-phase HZO grain while oxygenating under positive bias followed through iDPC-STEM images, where both cations and oxygen columns are displayed. The image of the virgin state at 0 V shows two red arrows pointing to two oxygen columns in the (100) planes neighboring a cationic column. Multislice iDPC-STEM image simulations of the r-phase ($R3m$ symmetry) in the inset shows the good match with the observations. (B) Out-of-plane displacement of \tilde{V}_o (in picometers) with external bias, in the marked supercell (red box) with respect to the positions in (A). Negative values indicate displacement toward bottom electrode. \tilde{V}_o shows both in-plane and out-of-plane

(toward bottom electrode) components (inset). (C) A new grain nucleates in the same region at 4 V, giving rise to a polycrystalline nature (FFT shown in inset). (D) Another region in the HZO film back at 0 V showing o-phase and m-phase (with multislice simulations of both in the insets). Note the change of orientation from [111] to [100]. (E) iDPC-STEM image of domains (mutually rotated by 180° about [111]) in the r-phase [to be compared with the simulation in the inset of figure 3A from (36)], which is retained when poled at -3 V (imaged at 0 V). Scale bars, 1 nm in (A), (C), and (E) and 2 nm in (D). Interfaces between the HZO and the top and bottom LSMO layers are marked in orange. In (D), only the HZO/bottom electrode interface is shown.

The m- and o-phases can be reversibly obtained again in subsequent cycles of positive bias (fig. S6D).

To elucidate the effects of device cycling with submillisecond pulses (35), we present results on tunnel junction Co/HZO (2 nm)/LSMO/STO devices switched between low-resistance state (LRS) and high-resistance state (HRS) at large voltages of ± 6 V. The devices showed an increasing TER (35) from 100% (stage A) to $10^6\%$ (stage B) upon cycling ~ 100 times (23, 44). An iDPC-STEM image from a selected region in the LSMO (bottom electrode) layer in the LRS (stage B) (Fig. 4A) shows a clear perovskite structure. In the HRS (stage B), however (Fig. 4B), Co inhomogeneously oxidizes exhibiting coexisting Co-rich and CoO_x -rich regions as revealed from the EDS analysis (fig. S7). This leaves oxygen-deficient LSMO in the BM-precursor phase. Thus, progression from stage A to stage B results in the gradual increase of CoO_x regions, an accumulated effect of oxygen voltammetry, which is reflected electrically in diverging resistance values.

To disentangle the short-term field effects on our devices from accumulated effects (35),

we report ex situ structure-property correlation results on ferroelectric capacitor stacks of LSMO (or TiN)/HZO (7 nm)/LSMO/STO cycled at 1 kHz fewer than 10 times at 5.5 V. The intrinsic P_r of our virgin devices in r-phase obtained from atomic displacements (35) (fig. S5B) is $< 9 \mu\text{C}/\text{cm}^2$, which is very small compared with the $35 \mu\text{C}/\text{cm}^2$ that were measured from polarization-voltage (P - V) loops at room temperature (7). This discrepancy is already an indication that most of the switching charge is intertwined with extrinsic factors. From the P - V hysteresis loops at various temperatures (Fig. 4C), we observed that, contrary to what is expected in classical ferroelectrics, the P_r increases with increasing temperature in the range from 150 to 300 K (22). This observation is in line with the polarization switching being correlated to the thermally activated oxygen-migration mechanism. These devices were prepared in a “down-polarized” configuration (5.5 V, 1 kHz) and imaged. The iDPC-STEM images clearly reveal the oxygen-deficient BM-precursor phase in the bottom LSMO layer close to the HZO interface (Fig. 4D) as also confirmed by corresponding disorderly oscillations in the c' parameter (Fig. 4D, inset).

Close to the STO interface, we found exaggerated oxygen octahedral tilts with Mn-O-Mn bond angles $< 146^\circ$ (marked in fig. S8A), which is the same interfacial feature observed during in situ STEM DC (direct current) testing at 2 V (fig. S2B). These observations also suggest that such extreme tilts initiate the transformation from perovskite to BM-precursor phase. These incipient oxygen migration-induced topotactic structural transitions result from the discharge of \tilde{V}_o in the electrodes. This thermally activated process leads to a built-in field at lower temperatures, which decreases as the temperature rises (fig. S8, B and C). The HZO layer, however, remains in an r-phase (Fig. 4E), revealing that it just acts as a conduit of oxygen between the source and sink (both reactive) electrodes in the short term.

We conducted comparative operando synchrotron nanobeam diffraction on Au/HZO/LSMO and LSMO/HZO/LSMO capacitors to answer the question of whether oxygen voltammetry can still occur if HZO is interfaced with a nonreactive electrode in the short term (35) (figs. S9 and S10). Both devices showed ferroelectric switching peaks (Fig. 4C and fig. S10), and we cycled them at 100 Hz in a

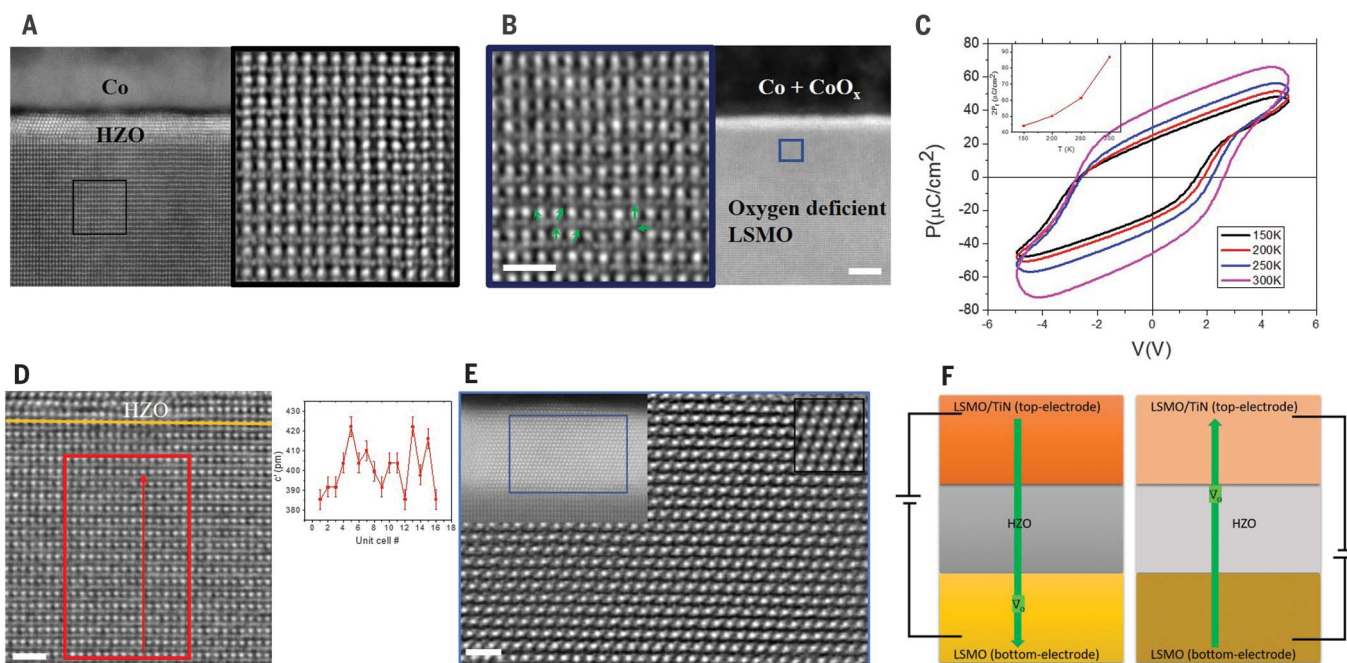


Fig. 4. Cycled tunnel junctions and ferroelectric capacitors. (A) Co/HZO (2 nm)/LSMO tunnel junction in LRS (500 μ s, 100 s of cycles poled at -6 V). A HAADF-STEM image is shown on the left (scale bar, 5 nm), and an iDPC-STEM image of a selected region in the LSMO is shown on the right (scale bar, 1 nm). (B) Ex situ imaging of tunnel junction in HRS (500 μ s, 100 s of cycles, poled at 6 V). (Right) HAADF-STEM (and corresponding information from EDS) shows CoOx/HZO/LSMO stack (scale bar, 5 nm). (Left) iDPC-STEM of a region in LSMO shows BM-precursor phase (scale bar, 1 nm). Selected Mn column displacements toward a square pyramidal geometry are marked by green arrows. (C) Temperature-dependent P - V loops obtained from dynamic hysteresis measurements at 1 kHz in LSMO/HZO (7 nm)/LSMO (30 nm) capacitors. Inset shows the

corresponding $2P_r$ versus T (temperature) curve (see also fig. S8). (D) iDPC-STEM image of LSMO close to the HZO interface (marked in orange) in TiN/HZO (7 nm)/LSMO capacitors, prepared in a down-polarized state (at 5.5 V). BM-precursor phase is formed, confirmed by disorder in the c' parameter (inset). (E) iDPC-STEM image of a down-polarized HZO layer, which is structurally still in r -phase. The left inset shows a HAADF-STEM image with the iDPC-STEM image presented for the region in the blue box, and the right inset shows a multislice simulation of the $R3m$ phase. Scale bar, 1 nm in (D) and (E). (F) Schematic of the polarity-dependent oxygen voltammetry process in the metal-insulator-metal device structure. Oxygen-deficient phases in various layers are represented with lighter colors.

modest voltage range between -3.5 and 3.5 V for tens of thousands of cycles (fig. S10C). In LSMO/HZO/LSMO devices, the virgin state and cycled state do not show any substantial differences in the HZO lattice parameter, which indicates the persistence of the r -phase during cycling (fig. S10D). However, in the case of Au/HZO/LSMO, we show that an m -phase (with a Bragg peak at $2\theta = 24.9^\circ$) appears after cycling and coexists with the r -phase (fig. S10, E and F). This reveals that the HZO layer itself is forced to act as source and sink of oxygen vacancies in the short term (35) when Au is used as a top electrode, which results in reversible structural phase transitions between the r - and m -phases. Further DC biasing results in an increase of m -phase fraction increasing positive bias, in agreement with the long-term in situ transmission electron microscopy (TEM) observations (fig. S11).

Using the model system of epitaxial HZO/LSMO/STO, we demonstrate that oxygen voltammetry and ferroelectric switching are intertwined (Fig. 4F) (35). With reactive top electrodes such as TiN (45), Co, and LSMO,

the HZO layer acts as a mere conduit for reversible oxygen migration between the electrodes, with incipient topotactic transformations taking place in them. With a noble top electrode (Au), HZO instead itself acts as a sink and source of \ddot{V}_O . In the longer term, redox-based phase-transition effects that follow oxygen migration in both HZO and LSMO become more marked. Although we remain agnostic about the nature of coupling between voltammetry and polarization switching, recent predictions of electrochemical origin of ferroelectricity in hafnia-based compounds (29), as well as demonstrations of giant electrostriction in the sister compound Gd:CeO₂ (46), can provide important clues.

In the context of tunnel junction devices, perovskite manganites (47) are routinely used as back electrodes (24–27, 48). Their crucial role as oxygen-conducting memristive layers (41) actively participating in charge transport is being recognized (35), with recent seminal demonstrations in ferroelectric tunnel junctions (28). Thus, our results have deep implications not just for hafnia-based ferro-

electrics, but also for the wider field of oxide electronics.

REFERENCES AND NOTES

1. T. S. Böschke, J. Müller, D. Bräuhäus, U. Schröder, U. Böttger, *Appl. Phys. Lett.* **99**, 102903 (2011).
2. A. Chernikova et al., *ACS Appl. Mater. Interfaces* **8**, 7232–7237 (2016).
3. X. Tian et al., *Appl. Phys. Lett.* **112**, 102902 (2018).
4. S. S. Cheema et al., *Nature* **580**, 478–482 (2020).
5. U. Schröder, C. S. Hwang, H. Funakubo, Eds., *Ferroelectricity in Doped Hafnium Oxide* (Woodhead Publishing, ed. 1, 2019).
6. P. Nukala et al., *Ferroelectrics* **569**, 148–163 (2020).
7. Y. Wei et al., *Nat. Mater.* **17**, 1095–1100 (2018).
8. R. Materlik, C. Kuneth, A. Kersch, *J. Appl. Phys.* **117**, 134109 (2015).
9. S. J. Kim, J. Mohan, S. R. Summerfelt, J. Kim, *JOM* **71**, 246–255 (2019).
10. T. Mimura, T. Shimizu, H. Funakubo, *Appl. Phys. Lett.* **115**, 032901 (2019).
11. X. Xu et al., *Nat. Mater.* 10.1038/s41563-020-00897-x (2021).
12. Y. Zhou et al., *Comput. Mater. Sci.* **167**, 143–150 (2019).
13. H. Mulaosmanovic et al., *ACS Appl. Mater. Interfaces* **9**, 3792–3798 (2017).
14. M. Pešić et al., *J. Comput. Electron.* **16**, 1236–1256 (2017).
15. N. Gong et al., *Appl. Phys. Lett.* **112**, 262903 (2018).
16. P. Buragohain et al., *Appl. Phys. Lett.* **112**, 222901 (2018).

17. S. Migita *et al.*, *Jpn. J. Appl. Phys.* **57**, 04FB01 (2018).
18. Y. H. Lee *et al.*, *Adv. Electron. Mater.* **5**, 180436 (2019).
19. T. Schenk *et al.*, *ACS Appl. Mater. Interfaces* **7**, 20224–20233 (2015).
20. H.-J. Lee *et al.*, *Science* **369**, 1343–1347 (2020).
21. C. Li *et al.*, *Nano Res.* **8**, 3571–3579 (2015).
22. S. U. Sharath *et al.*, *Adv. Funct. Mater.* **27**, 1700432 (2017).
23. Y. Wei *et al.*, *npj Quantum Mater.* **4**, 62 (2019).
24. M. C. Sulzbach *et al.*, *Adv. Electron. Mater.* **6**, 1900852 (2020).
25. M. Hambe *et al.*, *Adv. Funct. Mater.* **20**, 2436–2441 (2010).
26. D. Pantel, S. Goetze, D. Hesse, M. Alexe, *ACS Nano* **5**, 6032–6038 (2011).
27. S. Boyn *et al.*, *Nat. Commun.* **8**, 14736 (2017).
28. V. Rouco *et al.*, *Nat. Commun.* **11**, 658 (2020).
29. V. Mikheev *et al.*, *ACS Appl. Mater. Interfaces* **11**, 32108–32114 (2019).
30. M. D. Glinchuk *et al.*, *J. Alloys Compd.* **830**, 153628 (2020).
31. M. Qian, I. Fina, M. C. Sulzbach, F. Sánchez, J. Fontcuberta, *Adv. Electron. Mater.* **5**, 1800646 (2019).
32. C. Ferreyra *et al.*, *Phys. Rev. Appl.* **14**, 044045 (2020).
33. M. Pešić *et al.*, *Adv. Funct. Mater.* **26**, 4601–4612 (2016).
34. P. Gao *et al.*, *Nat. Commun.* **2**, 591 (2011).
35. Materials and methods are available as supplementary materials online.
36. S. de Graaf, J. Momand, C. Mitterbauer, S. Lazar, B. J. Kooi, *Sci. Adv.* **6**, eaay4312 (2020).
37. G. Sanchez-Santolino *et al.*, *Microsc. Microanal.* **20**, 825–831 (2014).
38. S. Stølen, E. Bakken, C. E. Mohn, *Phys. Chem. Chem. Phys.* **8**, 429–447 (2006).

39. P. Nukala *et al.*, *Appl. Phys. Lett.* **118**, 062901 (2021).
40. L. Cao *et al.*, *Adv. Mater.* **31**, 1806183 (2019).
41. L. Yao, S. Inkinen, S. van Dijken, *Nat. Commun.* **8**, 14544 (2017).
42. C. Baeumer *et al.*, *Nat. Commun.* **6**, 8610 (2015).
43. L. Bégon-Lours *et al.*, *Phys. Rev. Mater.* **4**, 043401 (2020).
44. Y. Wei *et al.*, *Phys. Rev. Appl.* **12**, 031001 (2019).
45. W. Hamouda *et al.*, *Appl. Phys. Lett.* **116**, 252903 (2020).
46. S. Santucci, H. Zhang, S. Sanna, N. Pyrds, V. Esposito, *J. Mater. Chem. A* **8**, 14023–14030 (2020).
47. A. Herpers *et al.*, *Adv. Mater.* **26**, 2730–2735 (2014).
48. G. Radaelli *et al.*, *Adv. Mater.* **27**, 2602–2607 (2015).
49. P. Nukala *et al.*, Dataset: Reversible oxygen migration and phase transitions in hafnia-based ferroelectric devices, version 1.0, Dataverse NL (2021); <https://doi.org/10.34894/EIOXPT>.

ACKNOWLEDGMENTS

Funding: P.N. acknowledges funding from European Union's Horizon 2020 research and innovation program under Marie Skłodowska-Curie grant agreement no. 794954 (nickname: FERHAZ). M.A., Y.W., B.K., and B.N. acknowledge the financial support of the CogniGron research center and the Ubbo Emmius Funds (University of Groningen). Y.W. and S.M. acknowledge a China Scholarship Council grant and a Van Gogh travel grant. We acknowledge MAX IV Laboratory for time on Beamline NanoMAX under proposal 20190954. Research conducted at MAX IV, a Swedish national user facility, is supported by the Swedish Research council under contract 2018-07152, the Swedish Governmental Agency for Innovation Systems under contract 2018-04969, and Formas under contract 2019-02496. S.M. acknowledges the French RENATECH network that supported the

cleanroom activity. P.N. acknowledges all the discussions with P. Buragohain from the University of Nebraska. **Author contributions:** P.N., B.N., M.A., and D.C. conceived the idea. P.N. synthesized the samples through PLD. M.A. and P.N. devised the in situ biasing device preparation protocol using FIB and made the devices. P.N., M.A., and S.d.G. set up the electrical biasing system compatible with Themis-Z microscope. P.N., M.A., and S.d.G. carried out the in situ biasing experiments with timely help from H.W.Z. and B.K.. Y.W. and S.M. synthesized and fabricated tunnel junction and capacitor devices and did the ex situ electrical testing. P.N. and M.A. prepared the lamellae and carried out imaging experiments. P.N., M.A., Y.W., T.C., and S.d.G. analyzed the TEM and transport data. D.C., A.B., and D.M. carried out the experiments on the beamline. E.S., P.N., D.C., and A.B. carried out synchrotron data analysis. All the authors discussed the data. P.N. and B.N. cowrote the manuscript, which was read, edited, and approved by all the authors. **Competing interests:** The authors declare no competing interests. **Data and materials availability:** The data are available from the University of Groningen data repository (49).

SUPPLEMENTARY MATERIALS

science.sciencemag.org/content/372/6542/630/suppl/DC1
Materials and Methods
Supplementary Text
Figs. S1 to S11
References (50–53)

22 October 2020; accepted 2 April 2021
Published online 15 April 2021
10.1126/science.abf3789

Reversible oxygen migration and phase transitions in hafnia-based ferroelectric devices

Pavan Nukala, Majid Ahmadi, Yingfen Wei, Sytze de Graaf, Evgenios Stylianidis, Tuhin Chakraborty, Sylvia Matzen, Henny W. Zandbergen, Alexander Björling, Dan Mannix, Dina Carbone, Bart Kooi and Beatriz Noheda

Science **372** (6542), 630-635.
DOI: 10.1126/science.abf3789originally published online April 15, 2021

A role for vacancies

Hafnia-based materials are of interest because of their potential use in microelectronic components. Hafnia-oxide is a ferroelectric material, but whether the polarization switching comes from the polar crystal phases or the migration of oxygen vacancies has remained an open question. Nukala *et al.* attempted to resolve this controversy by conducting electron microscopy during the operation of a hafnium zirconium oxide capacitor. The authors found that vacancy migration is intertwined with the ferroelectric switching, which has implications for the use of these materials in a range of microelectronic applications.

Science, this issue p. 630

ARTICLE TOOLS

<http://science.sciencemag.org/content/372/6542/630>

SUPPLEMENTARY MATERIALS

<http://science.sciencemag.org/content/suppl/2021/04/14/science.abf3789.DC1>

REFERENCES

This article cites 52 articles, 2 of which you can access for free
<http://science.sciencemag.org/content/372/6542/630#BIBL>

PERMISSIONS

<http://www.sciencemag.org/help/reprints-and-permissions>

Use of this article is subject to the [Terms of Service](#)

Science (print ISSN 0036-8075; online ISSN 1095-9203) is published by the American Association for the Advancement of Science, 1200 New York Avenue NW, Washington, DC 20005. The title *Science* is a registered trademark of AAAS.

Copyright © 2021 The Authors, some rights reserved; exclusive licensee American Association for the Advancement of Science. No claim to original U.S. Government Works